The role of suspended load transport in the occurrence of tidal sand waves

B. W. Borsje[1,2], W. M. Kranenburg[1], P. C. Roos[1], J. Matthieu[3,4], and S. J. M. H. Hulscher[1]

[1]Water Engineering and Management, University of Twente, Enschede, Netherlands, [2]Marine and Coastal Systems, Deltares, Delft, Netherlands, [3]Hydraulic Engineering, Deltares, Delft, Netherlands, [4]Water and Marine Engineering, Tetra Tech EBA, Vancouver, British Columbia, Canada

Abstract Tidal sand waves are dynamic bed patterns which are formed by the complex interaction between hydrodynamics, sediment transport, and geomorphology. Field data from the southern North Sea reveal that sand waves are absent where suspended load transport is the dominant transport mode. In order to understand the mechanisms responsible for the absence of sand waves, we study the influence of suspended load transport on the formation of tidal sand waves with a numerical process-based geomorphological model (Delft3D). Model simulations are presented in which the vertical eddy viscosity and sediment diffusivity are both spatially and temporally variable (k-ε turbulence model). First, it is shown that the preferred wavelength of sand waves for a relatively large grain size increases by the inclusion of suspended sediment, while for a relatively small grain size the flat bed is stable and no sand waves evolve. Second, it is shown that suspended load transport causes the suppression of long sand waves, resulting in a finite range of wavelengths that experience growth. Finally, by varying flow velocity amplitude and grain size, critical conditions for sand wave formation are found, i.e., conditions for which sand waves are marginally generated.

1. Introduction

Sand waves are rhythmic bed patterns which are found on the bed of sandy shallow seas. The wavelengths of these bed patterns are up to hundreds of meters, the heights are several meters, and the migration rates are up to several meters per year [*McCave*, 1971; *Terwindt*, 1971; *Huntley et al.*, 1993]. Sand waves are observed in many tide-dominated sandy shallow shelf seas like the North Sea, Bisanseto Sea, Irish Sea, the shelves off Spain and Argentina, and in many straits and tidal inlets around the world [*Van Santen et al.*, 2011, and references therein]. It is the combination of occurrence, dimensions, and dynamics that makes tidal sand waves a practically relevant marine bed pattern. In particular, due to their dynamic character, sand waves may interact with human activities like maintaining navigation channels and constructing pipelines and telecommunication cables [*Németh et al.*, 2003].

Field observations indicate a relation between suspended load transport and sand wave growth. *McCave* [1971] observed a northward decrease in sand wave height in a sand wavefield in front of the Dutch coast. He attributed this to a northward decrease in sediment size and consequently an increase in suspended load transport. Later, the damping effect of suspended load transport on sand wave growth was also found in observational studies worldwide by, e.g., *Rubin and McCulloch* [1980], *Ernstsen et al.* [2005], and *Buijsman and Ridderinkhof* [2008]. These observations motivate us to study the physical mechanisms responsible for the damping effect of suspended load transport on sand wave growth.

The formation of sand waves has been explained as a free instability of the sandy seabed subject to tidal motion. As first pointed out by *Hulscher* [1996], the interaction of the oscillatory tidal flow with sinusoidal bed perturbations gives rise to a tidally averaged residual flow, in the form of vertical recirculating cells directed from the trough to the crest of the sand wave. If the net displacement of the sediment dragged by this resulting flow pattern is directed toward the crests, the amplitude of the perturbation grows. On the other hand, the perturbation decays if the net motion of the sediment is directed toward the trough of the bed perturbation, i.e., decreasing the amplitude. The residual circulation induces a tide-averaged bed load sediment flux toward the crest of sand waves, which leads to sand wave growth. On the other hand, gravitational effects cause sediment to move more difficult upslope than downslope, creating a tide-averaged bed load sediment flux toward the trough and hence decay of the sand wave. The competition between these bed load sediment fluxes defines a preferred wavelength, which is referred to as the fastest-growing mode (FGM).

In the model by *Hulscher* [1996] only bed load transport is included, and the turbulent stresses are accounted for by combining a constant vertical eddy viscosity with a partial slip condition at the bed. *Komarova and Hulscher* [2000] extended the model of *Hulscher* [1996] by introducing a time dependency in the vertical eddy viscosity, while retaining only bed load transport. *Blondeaux and Vittori* [2005a, 2005b], *Besio et al.* [2006], and *Van Oyen and Blondeaux* [2009] introduced a depth-dependent eddy viscosity profile, which is time independent, and a no-slip condition at the bed. Moreover, suspended sediment dynamics were included in the model. The results of the model showed that sediment carried in suspension indeed provides a damping effect on the growth rate of sand waves. However, the physical mechanism responsible for the damping effect due to suspended load transport has not been explained yet.

Hulscher and Dohmen-Janssen [2005] argued that tidal sand waves and river dunes are comparable morphological features in terms of their processes. Therefore, studies into the formation of river dunes could point to possible physical mechanisms responsible for the damping effect of suspended load transport [*Engelund and Fredsøe*, 1982; *Colombini*, 2004; *Best*, 2005]. Analogous to tidal sand wave formation, several field studies have shown the damping effect of suspended load transport on river dune formation [*Chen and Nordin*, 1976; *Kostaschuk and Villard*, 1996; *Kostaschuk*, 2000]. As discussed by *Engelund and Fredsøe* [1982], it takes some time (and consequently distance) for the suspended sediment to adjust toward the equilibrium profile. Therefore, the maximum transport of suspended sediment occurs downstream of the crest of the bed form. Consequently, the gradient in the suspended load transport is positive at the crest, and therefore, the suspended load has a damping effect on the river dune formation. Whether this physical explanation is also applicable for tidal sand wave formation will be investigated in this paper.

Moreover, we are particularly interested in the physical mechanism behind the suppression of long sand waves. It is known from field observations that sand waves have a limited range in wavelengths [*Van Santen et al.*, 2011]. Whereas slope-induced transport is known to be able to suppress short sand waves, it is still an open question what mechanism suppresses the formation of long sand waves. Existing models fail to suppress the growth of very long sand waves [*Van den Berg et al.*, 2012]. As a direct result, while simulating the bottom evolution on a large spatial domain, the sand wavefield finally evolves toward one large bed form with a wavelength equal to the domain length [*Van den Berg et al.*, 2012]. This indicates that the essential physical mechanisms are not yet fully described. As shown by *Borsje et al.* [2013], the spatially and temporally variable vertical eddy viscosity (k-ε turbulence model) leads to much smaller growth rates for long sand waves compared to stability sand wave models in which the vertical eddy viscosity is time independent. However, positive growth rates for long sand waves are still obtained. Whether the inclusion of suspended sediment in combination with a k-ε turbulence model will lead to negative growth rates for long sand waves will also be investigated in this paper.

The aim of this paper is twofold. First, we aim to further investigate the relation between suspended load transport and the occurrence of sand waves by analyzing field data. Secondly, we aim to understand how suspended load transport mechanisms influence the formation of sand waves with the help of a numerical process-based geomorphological model (Delft3D).

2. Field Data on Sand Wave Occurrence and Transport Regime

Field observations suggest a relation between the sediment transport regime and the occurrence of sand waves [*McCave*, 1971]. To quantify the transport regime, we use the dimensionless Rouse number P [e.g., *Fredsøe and Deigaard*, 1992]. The Rouse number P is the ratio between the downward motion of the sediment due to gravity and the upward motion due to the water motion

$$P = \frac{w_s}{\kappa u_*}, \tag{1}$$

where w_s is the settling velocity of the sediment, κ is the von Karman constant (0.41), and u_* is the shear velocity. For the settling velocity of sediment w_s, we use the relation given by *Van Rijn* [1993] for a grain size d between 0.1 and 1 mm

$$w_s = \frac{10 v_w}{d} \left(\sqrt{1 + \frac{0.01(\rho_s/\rho_w - 1)gd^3}{v_w{}^2}} - 1 \right). \tag{2}$$

In equation (2), v_w is the kinematic viscosity coefficient of water, ρ_s is the specific density of the sediment, ρ_w is the density of water, and g is the gravitational acceleration.

The shear velocity u_* is defined by

$$u_* = \sqrt{\frac{\tau_b}{\rho_w}}, \tag{3}$$

where τ_b is the bed shear stress, which is calculated by

$$\tau_b = \frac{\rho_w g U_{M2}{}^2}{C^2}, \tag{4}$$

where U_{M2} is the amplitude of the M_2 tidal velocity and C is the Chézy roughness coefficient. The latter is calculated by

$$C = 18 \log\left(\frac{12H}{k_s}\right), \tag{5}$$

where k_s is the bottom roughness height and H the local water depth. Because most sand waves are covered with megaripples [*Tobias*, 1989; *Van Santen et al.*, 2011], we use the megaripple predictor proposed by *Van Rijn* [1993] to calculate the bottom roughness height k_s

$$k_s = 1.1\Delta_s(1 - \exp(-25\Delta_s/\lambda_s)), \tag{6}$$

where Δ_s is the megaripple height and λ_s is the megaripple length. Following *Van Santen et al.* [2011], we take $\Delta_s = 0.2$ m and $\lambda_s = 10$ m.

The different transport regimes are classified as follows [*Fredsøe and Deigaard*, 1992]:

$P < 1.2$	suspended load transport
$1.2 < P < 2.5$	incipient suspended load transport
$P > 2.5$	bed load transport

In order to calculate the local Rouse numbers P, we use the field data provided by *Borsje et al.* [2009a] on flow velocity amplitude U_{M2}, mean water depth H_0, and sediment grain size d. The field data are transformed to a uniform grid of 2×2 km for the Dutch continental shelf [*Borsje et al.*, 2009b]. The locations of sand wave fields on the Dutch continental shelf are provided by *Hulscher and Van den Brink* [2001], based on geological charts by the Dutch Geological Service and sand wave data from *Van Alphen and Damoiseaux* [1989].

All three transport regimes are present at the Dutch continental shelf (Figure 1a). However, the sand wavefields are characterized by Rouse numbers P closer to the bed load transport regime, and sand waves are hardly found where (incipient) suspended load transport is dominant (Figure 1b).

Additionally, we calculated the Rouse number P for 32 locations where sand wave fields are observed around the world, for which the tidal flow velocity amplitude U_{M2}, mean water depth H_0, and sediment grain size d are known. From these 32 locations, 23 are in the Dutch part of the North Sea [*Van Santen et al.*, 2011], 7 are in the Belgian part of the North Sea [*Cherlet et al.*, 2007], 1 is in San Francisco Bay in the U.S. [*Sterlini et al.*, 2009], and 1 is in the Gulf of Cadiz in Spain [*Németh et al.*, 2007]. The Rouse numbers P at these locations are between 1.9 and 5.0, which is comparable to the range in Rouse numbers P presented in Figure 1b.

3. Model Description

3.1. Hydrodynamics

The formation of sand waves is modeled using the numerical process-based geomorphological model Delft3D [*Lesser et al.*, 2004]. The model description is discussed in detail in *Borsje et al.* [2013]. In this paper we only summarize the most important equations and focus on the description of suspended sediment dynamics.

The system of equations consists of a horizontal momentum equation, a continuity equation, a turbulence closure model, a sediment transport equation, an advection–diffusion transport equation, and a sediment continuity equation. The vertical momentum equation is reduced to the hydrostatic pressure relation as vertical accelerations are assumed to be small compared to gravitational acceleration. The model equations are solved by applying sigma layering in the vertical. In this study, the model is run in the two-dimensional
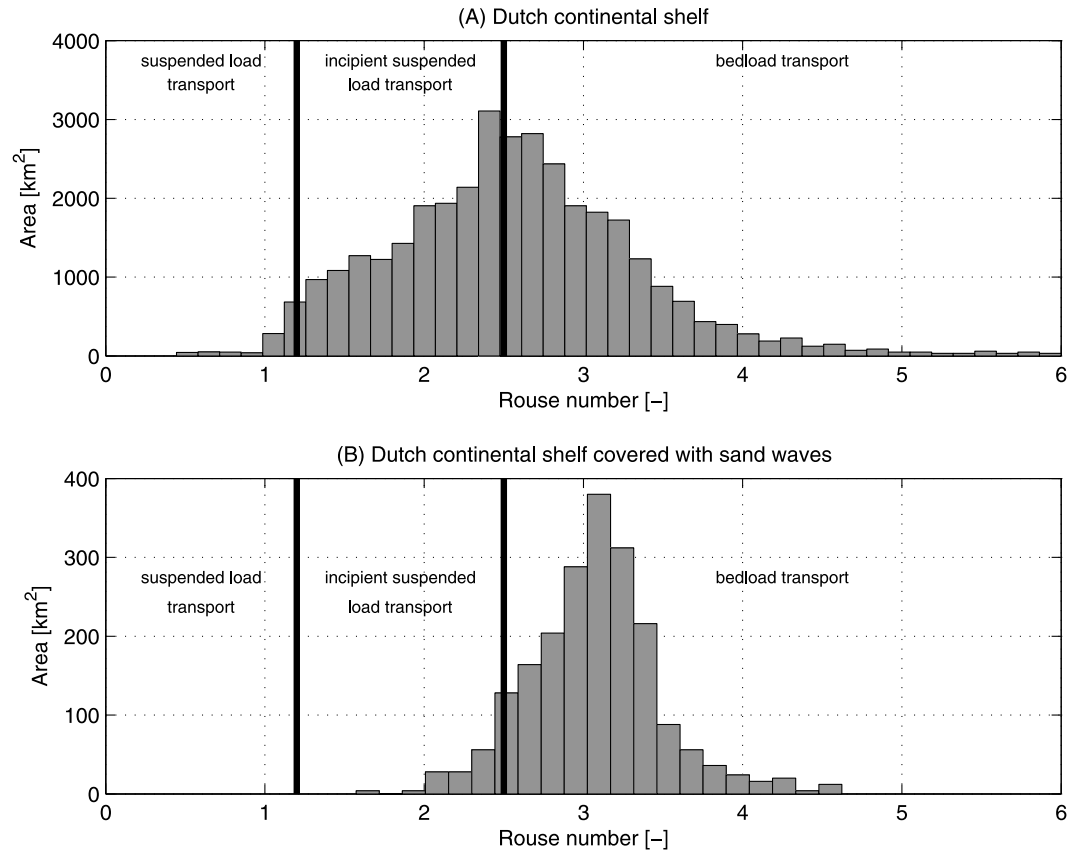
Figure 1. Distribution of the Rouse number P (a) over the Dutch continental shelf and (b) over the sand wave fields observed on the Dutch continental shelf. Distinction is made between three different transport regimes [*Fredsøe and Deigaard*, 1992].

vertical (2DV) mode, i.e., considering flow and variation in x and z direction only, while assuming zero flow and uniformity in y direction and ignoring Coriolis effects. At the length scales of sand waves, Coriolis effects have been shown to have a negligible effect [*Hulscher*, 1996].

In terms of the σ coordinates, the 2DV hydrostatic shallow water equations are described by

$$\frac{\partial u}{\partial t} + u\frac{\partial u}{\partial x} + \frac{\omega}{(H+\zeta)}\frac{\partial u}{\partial \sigma} = -\frac{1}{\rho_w}P_u + F_u + \frac{1}{(H+\zeta)^2}\frac{\partial}{\partial \sigma}\left(v\frac{\partial u}{\partial \sigma}\right),\tag{7}$$

$$\frac{\partial \omega}{\partial \sigma} = -\frac{\partial \zeta}{\partial t} - \frac{\partial[(H+\zeta)u]}{\partial x}.\tag{8}$$

Here u is the horizontal velocity, ω is vertical velocity relative to the moving vertical σ plane, ρ_w is the water density, H water depth below reference datum, ζ is the free surface elevation, P_u the hydrostatic pressure gradient, F_u describes the horizontal exchange of momentum due to turbulent fluctuations, and v the vertical eddy viscosity. The vertical eddy viscosity v is calculated by means of the k-ε turbulence closure model in which both the turbulent energy k and the dissipation ε are computed [*Rodi*, 1984]. The resulting vertical eddy viscosity v is variable both in time and space. For details on the k-ε turbulence model formulations, see *Burchard et al.* [2008].

At the bed ($\sigma = -1$), a quadratic friction law is applied and the vertical velocity ω is set to zero

$$\tau_b \equiv \rho_w\frac{v}{(H+\zeta)}\frac{\partial u}{\partial \sigma} = \rho_w u_* |u_*|, \omega = 0,\tag{9}$$

in which τ_b is the bed shear stress and u_* is the shear velocity that relates the velocity gradient at the bed to

the velocity u in the lowest computational grid point by assuming a logarithmic velocity profile (please note the difference between equations (4) and (9)).

At the free surface ($\sigma = 0$), a no-stress condition is applied and the vertical velocity ω is set to zero

$$\rho_w \frac{\upsilon}{(H + \zeta)} \frac{\partial u}{\partial \sigma} = 0, \omega = 0. \tag{10}$$

3.2. Sediment Transport and Bed Evolution

The bed load transport, S_b is calculated by *Van Rijn et al.* [2004]

$$S_b = 0.006\alpha_s \rho_s w_s d M^{0.5} M_e^{0.7}, \tag{11}$$

where α_s is a correction parameter for the slope effects (see below), ρ_s is the specific density of the sediment, w_s is the settling velocity of the sediment, and d the sediment grain size. M and M_e, respectively the sediment mobility number and excess sediment mobility number, are given by

$$M = \frac{u_r^2}{(\rho_s/\rho_w - 1)gd}, M_e = \frac{(u_r - u_{cr})^2}{(\rho_s/\rho_w - 1)gd}, \tag{12}$$

where u_r is the magnitude of the equivalent depth-averaged velocity computed from the velocity in the bottom computational layer assuming a logarithmic velocity profile, u_{cr} is the critical depth-averaged velocity for the initiation of motion of sediment based on the Shields curve. If $u_r < u_{cr}$, the bed load transport is set to zero.

Bed load transport is affected by bed level gradients, which causes sediment to move more difficult upslope than downslope. The correction parameter α_s for the slope effect is usually taken inversely proportional to the tangent of the angle of repose of sand φ_s [*Sekine and Parker*, 1992]

$$\alpha_s = \frac{1}{\tan\varphi_s}. \tag{13}$$

The angle of repose of sand φ_s is in the range between 15° and 30°. In this paper we set α_s equal to 2.5, following *Van den Berg et al.* [2012]. This value corresponds to an angle of repose of sand of 22°. For sediment transported upslope the value of $\alpha_s = -2.5$, and for sediment transported downslope the value of $\alpha_s = 2.5$.

The suspended sediment concentration is calculated by solving the advection–diffusion equation

$$\frac{\partial c}{\partial t} + \frac{\partial (cu)}{\partial x} + \frac{\partial (w - w_s)c}{\partial z} = \frac{\partial}{\partial x}\left(\varepsilon_{s,x}\frac{\partial c}{\partial x}\right) + \frac{\partial}{\partial z}\left(\varepsilon_{s,z}\frac{\partial c}{\partial z}\right), \tag{14}$$

where c is the mass concentration of sediment and $\varepsilon_{s,x}$ and $\varepsilon_{s,z}$ are the sediment diffusivity coefficients in x and z direction, respectively. The horizontal sediment diffusivity $\varepsilon_{s,x}$ and vertical sediment diffusivity $\varepsilon_{s,z}$ are taken equal to the horizontal and vertical eddy viscosity, respectively.

Suspended sediment includes all sediments transported above the reference height, $a = 0.01H$. The reference concentration, c_a, at height a is given by *Van Rijn* [2007]

$$c_a = 0.015\rho_s \frac{dT_a^{1.5}}{aD_*^{0.3}}. \tag{15}$$

Here T_a is the nondimensional bed shear stress

$$T_a = \frac{\mu\tau_b - \tau_{cr}}{\tau_{cr}}, \tag{16}$$

where μ is the efficiency factor, which is the ratio between the grain-related friction factor and the total

current-related friction factor, τ_{cr} the critical bed shear stress for the initiation of motion of sediment, and D_* is the nondimensional particle diameter. Details on the calculation of the efficiency factor, critical bed shear stress, and nondimensional particle diameter can be found in *Apotsos et al.* [2011]. At the free surface, the vertical diffusive fluxes are set to zero. Details on the calculation of the suspended sediment concentration profile in the Delft3D model are given by *Deltares* [2014].

Finally, the bed evolution is governed by the sediment continuity equation (Exner equation), which reads

$$\left(1 - \varepsilon_p\right)\frac{\partial z_b}{\partial t} + \frac{\partial(S_b + S_s)}{\partial x} = 0, \tag{17}$$

in which $\varepsilon_p = 0.4$ is the bed porosity, S_b is the bed load transport (equation (11)), and S_s is the suspended load transport calculated by

$$S_s = \int_a^{(H+\zeta)} \left(uc - \varepsilon_{s,z}\frac{\partial c}{\partial x}\right)dz. \tag{18}$$

Sediment transported below the reference height a is regarded as bed load sediment transport, as it responds almost instantaneously to changing flow conditions [*Van Rijn*, 2007].

Equation (17) simply states that convergence (or divergence) of the total transport rate must be accompanied by a rise (or fall) of the bed profile.

3.3. Model Setup

In the horizontal dimension, the model domain is 50 km, with a variable horizontal resolution. In the center of the model domain the grid size is 10 m, increasing to a value of 1500 m at the lateral boundaries. In the vertical dimension, the model grid is composed of 20 layers, with small vertical resolution near the bed and increasing toward the water surface. At the lateral boundaries, a Riemann boundary condition is imposed [*Verboom and Slob*, 1984]. For this type of boundary condition, a depth-averaged velocity amplitude and a tidal frequency is imposed, and outgoing tidal waves are allowed to cross the open boundary without being reflected back into the computational domain. The tidal frequency σ_{M2} of the semidiurnal depth-averaged velocity amplitude U_{M2} is set at $1.45 \times 10^{-4}\,\text{s}^{-1}$. At the lateral boundaries, both the suspended sediment concentrations and bed load transport rates are set to zero. The hydrodynamic time step is 3 s, and after every hydrodynamic time step, the bed level is updated. The initial bed level perturbation z_b is prescribed as the product of a sinusoidal sand wave pattern with a given wavelength L and amplitude A together with an envelope function. This ensures a gradual transition from the flat bed to the sand wavefield in the center of the domain. Consequently, a coarser grid can be used near the boundaries. The initial amplitude of the sand wave $A_0 = 0.5$ m. Smaller initial amplitudes show the same quantitative behavior, only require more vertical layers, and are therefore more time consuming. The Chézy roughness coefficient C is calculated by equation (5). The model is run for two tidal cycles. The first tidal cycle is used for spin-up, and no bed level changes are allowed. During the second tidal cycle, bed level changes are allowed. Assuming exponential growth (which is valid for small-amplitude sand waves [*Besio et al.* 2008]), the growth rate γ_R for the bed perturbation is calculated by

$$\gamma_R = \frac{1}{T}\text{Re}\left\{\log\left(\frac{A_1}{A_0}\right)\right\}, \tag{19}$$

where T is the tidal period and A_1 is the bed amplitude of the sand wave after one tidal cycle of morphodynamic computation. Both A_0 and A_1 are determined by a fast Fourier transform of the central part of the sand wave domain. Positive values of γ_R indicate growth of the bottom perturbation, whereas negative values indicate decay.

A reference coordinate is introduced to describe the results of the model simulations. The crest of the sand wave is located at $x = 0$. The flood direction is from left to right, and the ebb direction is in the opposite direction. Maximum flood is the moment in time when the maximum depth-averaged velocity at the crest of the sand wave is reached during flood. The front and the rear of the sand wave are located at the left and right side of the crest of the sand wave, respectively.

Table 1. Overview of the Values and Dimensions of the Sets of Tidal Conditions

Description	Symbol	Value(s) of Tidal Conditions			Dimension
		Case I	Case II	Case III	
Amplitude of horizontal M_2 tidal velocity	U_{M2}	0.65	0.65	[0.65–0.8]	m s^{-1}
Mean water depth	H_0	25	25	25	m
Sediment grain size	d	0.2 and 0.35	0.2 and 0.35	[0.25–0.3]	mm
Wave number	k	$2\pi/600$	[0.4×10^{-3}–0.04]	[0.4×10^{-3}–0.04]	m^{-1}
Rouse number	P	1.4 and 3.0	1.4 and 3.0	[1.9–2.5]	—

4. Results

In the following model simulations, the effect of suspended load transport on the growth of tidal sand waves is presented. The dominant transport regime for the different model simulations is determined based on the classification given by *Fredsøe and Deigaard* [1992], as presented in section 2. The model was run for three different sets of tidal conditions (Table 1). The first set of tidal conditions (Case I) was a fixed flow velocity amplitude U_{M2}, mean water depth H_0, and wave number k and two different grain sizes d (corresponding to the bed load and the suspended load regime). In the second set of tidal conditions (Case II), the flow velocity amplitude U_{M2}, mean water depth H_0, and grain sizes d were taken the same as in Case I, only now the wave number k was varied in order to study the existence of a fastest-growing mode. In the third set of tidal conditions (Case III), both the flow velocity amplitude U_{M2} and the sediment grain size d were varied and critical conditions for sand wave growth were determined. The settings for flow velocity amplitude U_{M2}, mean water depth H_0, and grain size d resemble a typical North Sea situation for sand wave occurrence [*Borsje et al.*, 2009a].

4.1. Sediment Transport Rates

First, the model is run for two different grain sizes ($d = 0.2$ mm and $d = 0.35$ mm), a flow velocity amplitude $U_{M2} = 0.65$ m s^{-1}, a mean water depth $H_0 = 25$ m, and a sand wave with a wavelength $L = 600$ m (Case I). A grain size of $d = 0.35$ mm is the average grain size found in sand waves in the North Sea, whereas a grain size of $d = 0.2$ mm is smaller than the smallest grain size found in sand waves at the Dutch continental shelf [*Borsje et al.*, 2009a].

Focusing on the suspended sediment concentrations c during maximum flood, we observed higher suspended sediment concentrations c for the small grain sizes (Figure 2b) compared to the large grain sizes (Figure 2a). Moreover, sediment concentration maxima occur near the bed and decrease rapidly higher in the water column. Furthermore, a downstream shift is observed in the suspended sediment concentrations (the contour lines in Figure 2 are out of phase with the sand wave). The downstream shift is larger for small grain sizes compared to large grain sizes (i.e., the phase difference between the contour lines and the sand wave is larger for the small grain sizes). At a water depth of -16 m, the downstream shift is 25 m and 45 m for a grain size of $d = 0.35$ mm and $d = 0.2$ mm, respectively (Figure 2).
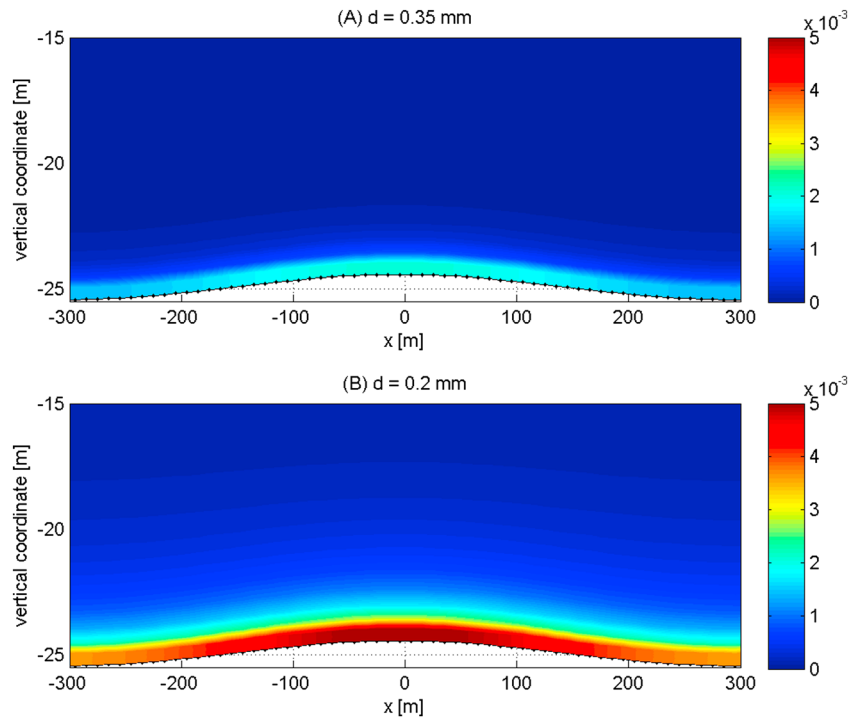
Concerning the tide-averaged suspended sediment concentrations (Figure 3), we observe higher tide-averaged suspended sediment concentrations $<c>$ above the crest than in the trough for both grain sizes. This difference is explained by the slightly higher flow velocities and therefore higher suspended sediment concentrations above the crest of the sand wave compared to the trough.

Next, we study the tide-averaged bed load transport rate $<S_b>$ and the tide-averaged suspended load rate $<S_s>$. The tide-averaged bed load transport rate $<S_b>$ is smaller for small grain sizes than for large grain sizes (Figure 4a). For decreasing grain sizes, both the sediment mobility number and the excess sediment mobility number increase (equation (12)). However, the total bed load transport rate decreases due to a decrease in settling velocity of sediment (equation (11)). Consequently, for decreasing grain sizes, the bed load transport rate slightly decreases and the sediment is dominantly transported in suspension (Figure 4b). Nevertheless, for decreasing grain sizes, the total sediment transport rate is increasing. Remarkably, the tide-averaged suspended load transport rate $<S_s>$ (Figure 4b) is opposite in sign compared to the tide-averaged bed load transport rate $<S_b>$ (Figure 4a). Since the divergence or convergence in transport rates determines the growth or decay of the sand wave (equation (17)), both transport mechanisms induce an opposite effect on sand wave formation. The bed load transport induces sand wave growth, and suspended load transport
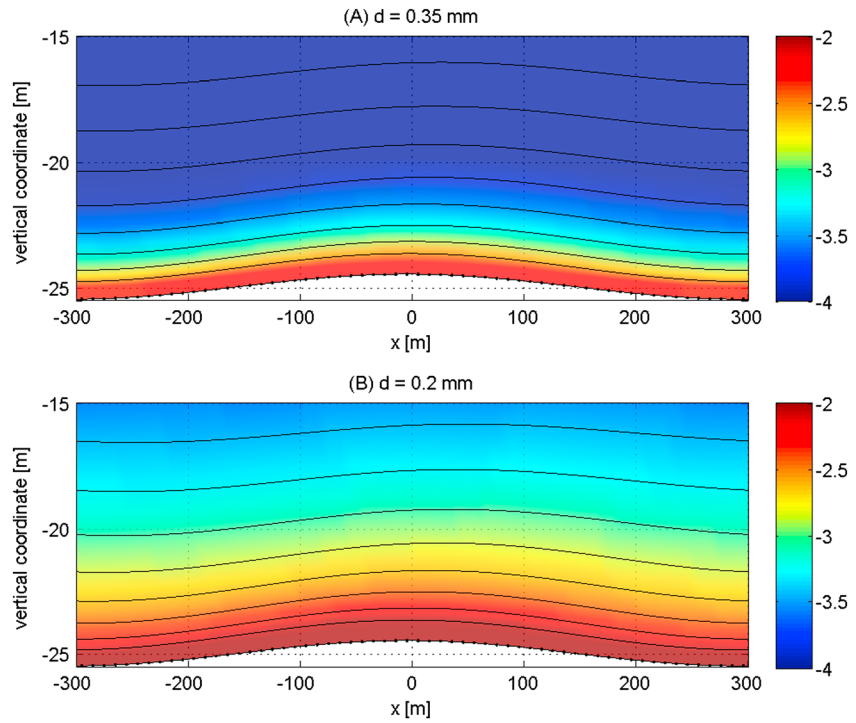
Figure 2. Suspended sediment concentrations log c (kg m^{-3}) during maximum flood (flow from left to right) for a sand wave with wavelength $L = 600$ m, (a) a grain size $d = 0.35$ mm (Rouse number $P = 3.0$), and (b) a grain size $d = 0.2$ mm (Rouse number $P = 1.4$). The sand wave crest is located at $x = 0$. For clarity, only the lowest 10 m of the water column is shown (Case I in Table 1). Contour lines are included to show the phase lag between the sediment concentration and the bed level.

Figure 3. Tide-averaged suspended sediment concentrations $<c>$ (kg m^{-3}) for a sand wave with wavelength $L = 600$ m, (a) a grain size $d = 0.35$ mm (Rouse number $P = 3.0$), and (b) a grain size $d = 0.2$ mm (Rouse number $P = 1.4$). The sand wave crest is located at $x = 0$. For clarity, only the lowest 10 m of the water column are shown (Case I in Table 1).
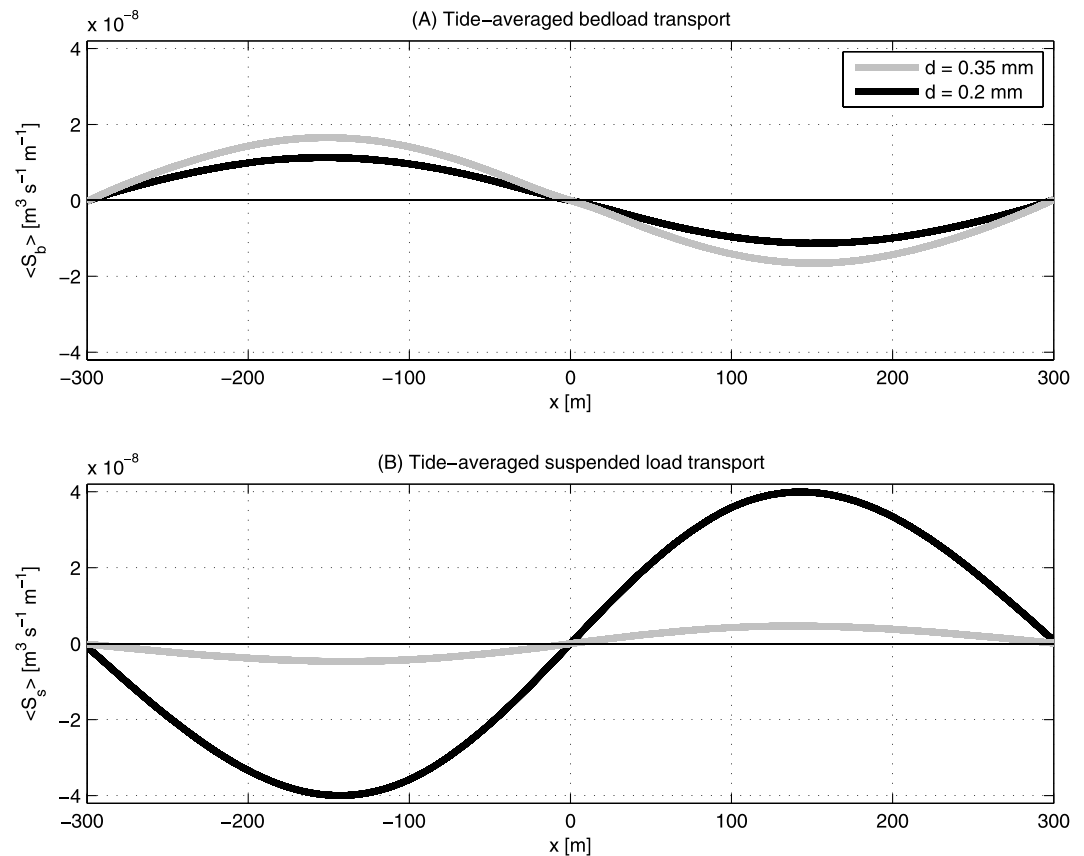
Figure 4. (a) Tide-averaged transport rates ($m^3 s^{-1} m^{-1}$) over a sand wave with wavelength $L = 600$ m, for (a) the bed load transport $< S_b >$ (including slope-induced transport) and (b) the suspended load transport $< S_s >$, for a grain size $d = 0.35$ mm (Rouse number $P = 3.0$) (gray line) and $d = 0.2$ mm (Rouse number $P = 1.4$) (black line) (Case I in Table 1).

provides a damping effect. For small grain sizes ($d = 0.2$ mm) the gradient in the tide-averaged suspended load transport $< S_s >$ is even larger than the gradient in the tide-averaged bed load transport rate $< S_b >$, inducing a decay of the sand wave, at least for this wavelength and tidal condition. As illustrated in Figure 4, tide-averaged bed load transport rates $< S_b >$ are much less sensitive to grain size variations compared to tide-averaged suspended load transport rates $< S_s >$.

4.2. Bed Evolution

Next, we study the damping effect of suspended load transport on the growth curve by varying the topographic wave number $k = 2\pi/L$, while keeping the flow velocity amplitude U_{M2} and mean water depth H_0 constant. In order to analyze the impact of suspended load, two distinct grain sizes are considered (Case II in Table 1). It is found that the damping effect of suspended load transport is the strongest for the largest wave numbers (Figures 5b and 6b). For a grain size of $d = 0.35$ mm, the contribution of the suspended load transport to the total growth rate is relatively small (compared to the bed load transport and the slope-induced transport). The fastest-growing mode is slightly influenced for relatively large grains. In particular, an increase is found from $L_{FGM} = 330$ m to $L_{FGM} = 400$ m by including suspended sediment (Figure 5).

Another interesting observation is the suppression of long sand waves for a relative large grain size (Figure 5e). Whereas the slope-induced transport suppresses very short sand waves, suspended sediment dynamics causes very long sand waves to decay. For this tidal condition we find a range in wavelengths with a positive growth rate between $L = 200$ m and $L = 4200$ m.

By decreasing the grain size, it appears that suspended load transport damps entirely the appearance of all bottom perturbations such that sand waves are absent, while considering only bed load a fastest-growing mode of $L_{FGM} = 370$ m is found (Figure 6).
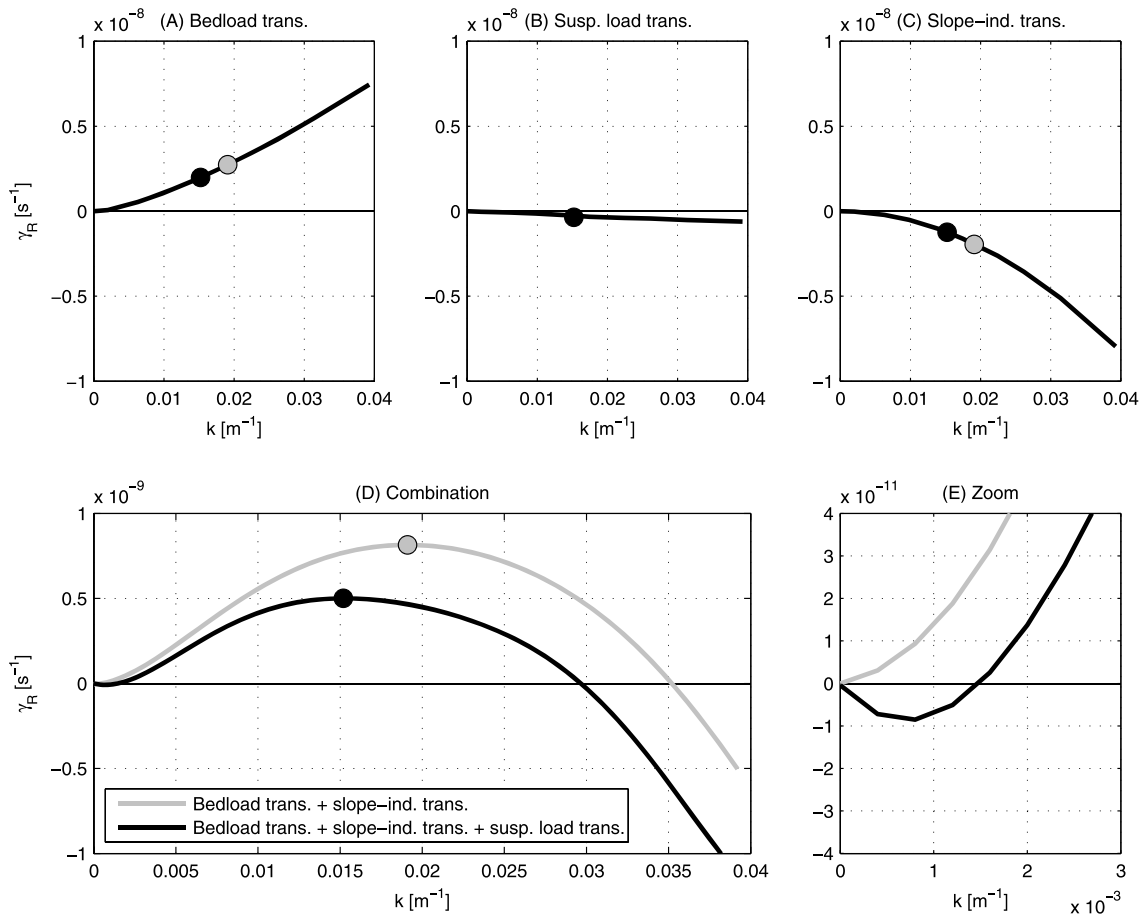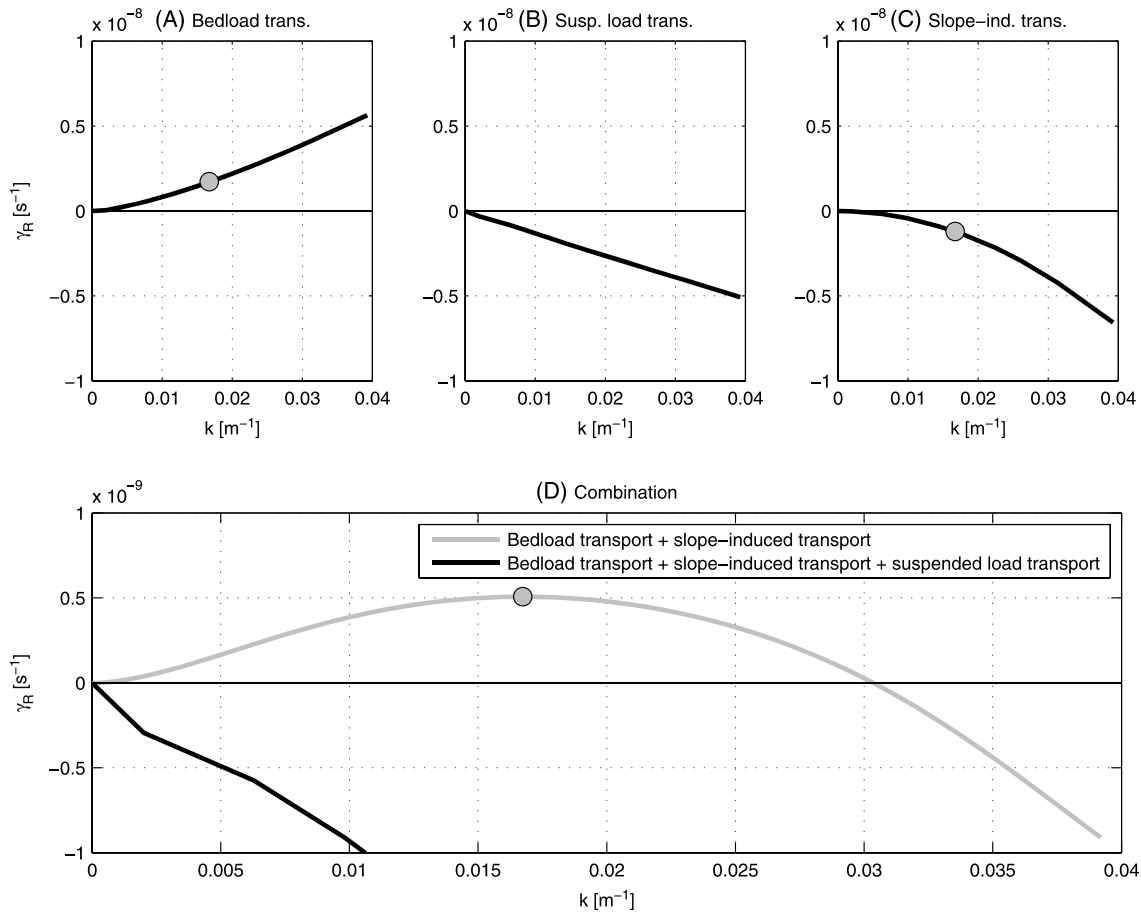
Figure 5. The total growth rate curve is the sum of (a) the bed load transport component, (b) the suspended load transport component, and (c) the slope-induced transport component for a grain size $d = 0.35$ mm (Rouse number $P = 3.0$). On the horizontal axis the wave number k (m^{-1}) is given, and on the vertical axis the growth rate γ_R (s^{-1}). The circles indicate the growth rates belonging to the fastest-growing mode L_{FGM}. (d) Distinction is made between the growth curve for a combination of the bed load transport component and slope-induced transport component (gray line) and a combination of the bed load transport component, suspended load transport component, and slope-induced transport component (black line). (e) A zoom of the total growth curve is given for small wave numbers k (Case II in Table 1).

4.3. Critical Conditions for Sand Wave Formation

The model results show negative growth rates for both long sand waves and short sand waves (Figure 5). This motivates us to investigate whether we can find critical conditions for sand waves formation. We start with a simulation for which the Rouse number $P = 2.5$ (lower limit of bed load transport regime) and vary successively the flow velocity amplitude U_{M2} and grain size d toward the suspended load transport regime according to the parameter range given in Table 1 (Case III). The parameter settings for the reference run (for which the Rouse number $P = 2.5$) is as follows: flow velocity amplitude $U_{M2} = 0.65$ m s^{-1}, mean water depth $H_0 = 25$ m, and grain size $d = 0.3$ mm. The Rouse number P is hardly dependent on the mean water depth H_0 and therefore taken constant in this analysis.

For the reference run, the fastest-growing mode $L_{FGM} = 540$ m and sand waves with a wavelength between $L = 290$ m and $L = 2500$ m show positive growth rates (Figure 7). By decreasing the grain size d, the fastest-growing mode L_{FGM} increases. The situation for which sand waves are marginally generated is for a grain size $d = 0.255$ mm (Figure 7b) and a corresponding Rouse number $P = 2.0$ (Figure 7a). For even smaller grain sizes, all bed perturbations are damped and the flat bed is stable.

Next, we increase the flow velocity amplitude U_{M2} and impose the grain size $d = 0.3$ mm and mean water depth $H_0 = 25$ m (Figure 8). Marginally generated sand waves are observed for a Rouse number $P = 2.0$ (Figure 8a). The critical flow velocity amplitude $U_{M2} = 0.775$ m s^{-1} for which sand waves are marginally generated (Figure 8b).

Figure 6. The total growth rate curve is the sum of (a) the bed load transport component, (b) the suspended load transport component, and (c) the slope-induced transport component for a grain size $d = 0.2$ mm (Rouse number $P = 1.4$). On the horizontal axis the wave number k [m^{-1}] is given, and on the vertical axis the growth rate γ_R (s^{-1}). The circles indicate the growth rates belonging to the fastest-growing mode L_{FGM}. (d) Distinction is made between the growth curve for a combination of the bed load transport component and slope-induced transport component (gray line) and a combination of the bed load transport component, suspended load transport component, and slope-induced transport component (black line) (Case II in Table 1).

In the field, sand wave occurrence was observed for a Rouse number $P > 1.9$ (section 2). Model simulations show comparable results: Sand waves are formed for Rouse numbers $P > 2.0$.

4.4. Physical Explanation

As found in the model simulations, the formation of sand waves is governed by three different transport processes: bed load transport, slope-induced transport, and suspended load transport. In this section, we give the physical explanation for the formation of sand waves, focusing on these three different transport processes (Figure 9).

During the flood phase, the bed load transport rate is slightly larger in front of the crest, compared to the rear of the crest due to the modulation of the flow velocity field as shown by *Hulscher* [1996]. During the ebb phase, the opposite effect is observed: larger bed load transport rates at the rear of the crests compared to the front of the crest. The net effect is a bed load sediment flux toward the crest of the sand waves, which leads to sand wave growth.

The slope-induced transport is smaller in front of the crest, compared to the rear of the crest during the flood phase, since sediment moves more easily downslope than upslope. During the ebb phase, the opposite effect is observed and the net effect is a sediment flux from the crest to the trough.

The suspended load transport is determined by the suspended sediment concentration and the flow velocity. During the flood phase, the suspended sediment concentration in front of the crest is smaller compared to the rear of the crest (as shown in Figure 2). Moreover, the flow velocities are slightly larger above the crest of the sand wave compared to the trough. As a consequence, the suspended load transport rate at the rear of the sand wave is larger than the suspended load transport at the front of
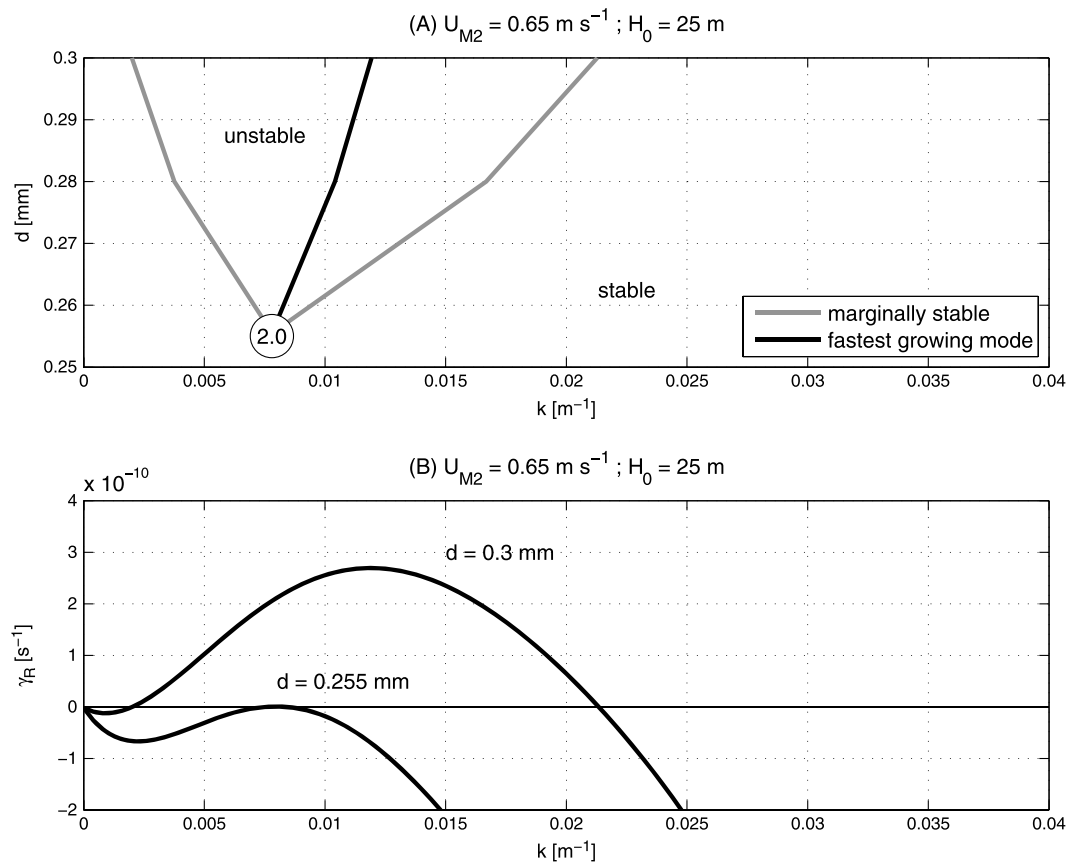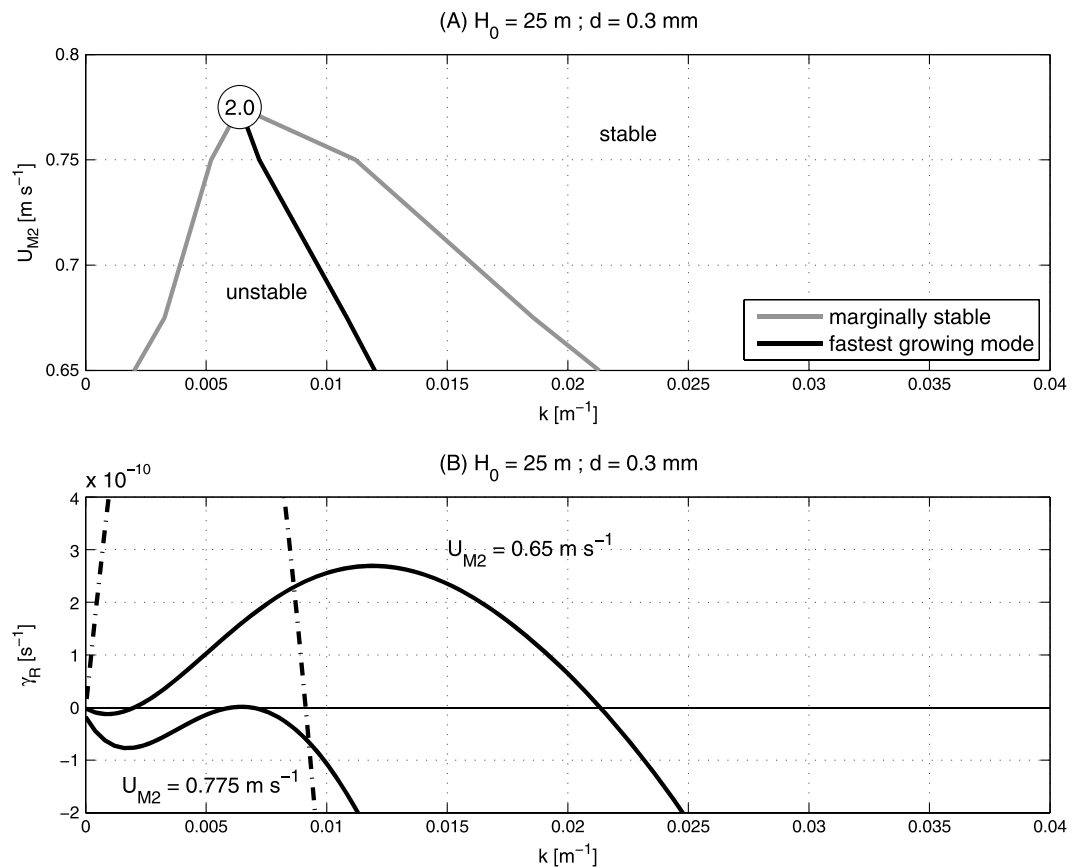
Figure 7. (a) Marginal stability condition (gray lines), which discriminates between positive growth rates (unstable) and negative growth rates (stable) as function of the wave number k (m^{-1}) for a variation in grain size d (mm). Other parameter values are given in the subplot title. The growth rate with the fastest-growing mode is indicated with the black line. The Rouse number P for the marginal stable condition is indicated in the circle (Case III in Table 1). (b) Two growth rate curves are shown: one for the reference run ($d = 0.3$ mm) and one for the conditions leading to marginal stable conditions ($d = 0.255$ mm).

the sand wave during the flood phase. During the ebb phase, the opposite is observed, and the net effect is a sediment flux from the crest to the trough of the sand wave.

The downstream shift in the suspended sediment concentration during flood is larger for small grain sizes, compared to large grain sizes, as shown in Figure 2. As a consequence, the gradient in suspended load transport is also larger for small grain sizes (Figure 4). At a certain point, for decreasing sediment grain sizes, the growth of the bed perturbation by the bed load sediment flux is counteracted by the decay of the bed perturbation by the slope-induced transport flux and the suspended load transport flux, and a critical condition for sand wave growth was found (Figure 7). The same explanation holds for increasing flow velocity amplitudes: The downstream shift in the suspended sediment concentration increases for increasing flow velocity amplitude. At a certain point, the suspended load transport flux and the slope-induced flux are larger than the bed load transport flux leading to a critical condition for sand wave growth (Figure 8). The impact of the inclusion of suspended load transport on sand wave growth is shown in Figure 10. In this figure, the fastest-growing mode is shown for a variation in flow velocity amplitude and hence the Rouse number, for the same parameter settings as the model simulation in Figure 8. Remarkably, the difference between the fastest-growing modes is considerable, even in the bed load regime.

5. Discussion

In this paper, we studied the relation between suspended load transport and the formation of sand waves, both in the field and in the numerical process-based geomorphological model Delft3D. In the field, sand wave fields

Figure 8. (a) Marginal stability condition (gray lines), which discriminates between positive growth rates (unstable) and negative growth rates (stable) as function of the wave number k (m^{-1}) for a variation in flow velocity amplitude U_{M2} (m s^{-1}). Other parameter values are given in the subplot title. The growth rate with the fastest-growing mode is indicated with the black line. The Rouse number P for the marginal stable condition is indicated in the circle (Case III in Table 1). (b) Two growth rate curves are shown: one for the reference run ($U_{M2} = 0.65$ m s^{-1}) and one for the conditions leading to marginal stable conditions ($U_{M2} = 0.775$ m s^{-1}). The dash-dotted line shows the growth curve for a constant eddy viscosity simulation and is included for later reference.

were only observed in regions where bed load was the dominant transport mode. Where suspended load was the dominant transport mode, sand waves were not observed. The same relation was found in model simulations, in which the effect of suspended load transport on sand wave formation and occurrence was studied. We found critical conditions for sand wave occurrence by using an advanced k-ε turbulence model with the inclusion of suspended sediment dynamics. A combination of an advanced turbulence model with suspended sediment dynamics has never been applied before in sand wave modeling.

The suppression of long sand waves was caused by the combination of an advanced turbulence model (k-ε turbulence model) and suspended load transport. To be conclusive, we also ran the model with a time-independent eddy viscosity (i.e., the constant eddy viscosity model used in *Borsje et al.* [2013]), with the same parameter settings as the reference run in Case III (dotted line in Figure 8b). In the constant eddy viscosity model simulation, the fastest-growing mode $L_{FGM} = 1378$ m, which is much larger compared to the reference run. The larger fastest-growing mode is caused by the overestimation in bed shear, as extensively discussed by *Borsje et al.* [2013]. Moreover, no suppression of long sand waves is observed for the constant eddy viscosity model. Also, no suppression of long sand waves was observed for sand wave models in which a time-independent vertical turbulence profile is adopted in combination with suspended sediment dynamics [*Blondeaux and Vittori*, 2005a, 2005b; *Besio et al.*, 2006; *Van Oyen and Blondeaux*, 2009].

Critical conditions for sand wave formation were presented earlier by *Komarova and Hulscher* [2000], who employed a linear stability analysis on a stability sand wave model in which only bed load transport was included. They used the slope parameter to control the unstable modes and found a critical mode

Bedload transport

Slope–induced transport

Suspended load transport
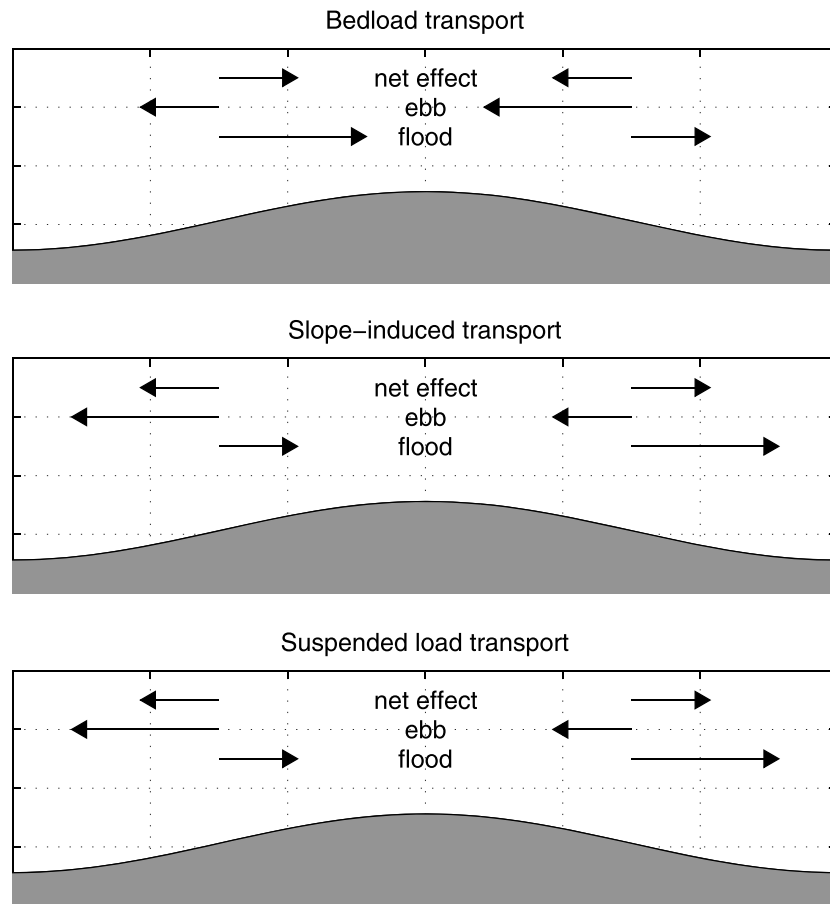
Figure 9. Schematic overview of the three dominant processes in sand wave formation: bed load transport, slope-induced transport, and suspended load transport. Distinction is made between the fluxes during the flood and the ebb phase. Fluxes and sand wave dimensions are not to scale.

of $L_{crit} = 571$ m for a mean water depth $H_0 = 45$ m and for a critical slope parameter $\alpha_s = 21$. In their model, a turbulence model (in which viscosity was mean water depth times near-bed velocity) is used in which the time dependency was crucial to find the critical conditions. This is in line with our result that the advanced k-ε turbulence model is able to generate critical conditions, whereas the constant eddy viscosity model is not able to do so. However, in our analysis we found critical conditions for more realistic parameter settings and with the inclusions of suspended sediment dynamics. Such a result was not presented in stability sand wave models including suspended sediment dynamics [*Blondeaux and Vittori*, 2005a, 2005b; *Besio et al.*, 2006; *Van Oyen and Blondeaux*, 2009].

In our simulations, we found that suspended load transport always has a damping effect on sand wave growth (Figure 9). However, *Van Oyen and Blondeaux* [2009] showed that sediment transported in suspension first lead to a positive effect on the growth rate of sand waves when only a slight increase of the depth-averaged tidal velocity is considered. By further increasing the depth-averaged tidal velocity, the relative importance of the suspended load transport became larger and the growth rate strongly decreased. The explanation for the contradiction in both model outcomes is not yet understood.

Now the formation of sand waves has been studied, a next step is to study the mechanisms which control the equilibrium height of sand waves. Moreover, the proposed model allows us to investigate whether the fastest-growing mode for a small-amplitude sand wave coincides with the wavelength of a sand wave in its equilibrium shape. Finally, starting from a flat bed with random small perturbations, the formation of a regular sand wavefield can be studied, while both long sand waves and short sand waves will be damped. Whether the wavelength of these regular sand waves are comparable to the fastest-growing mode found in the schematized situation still remains an important question to answer.
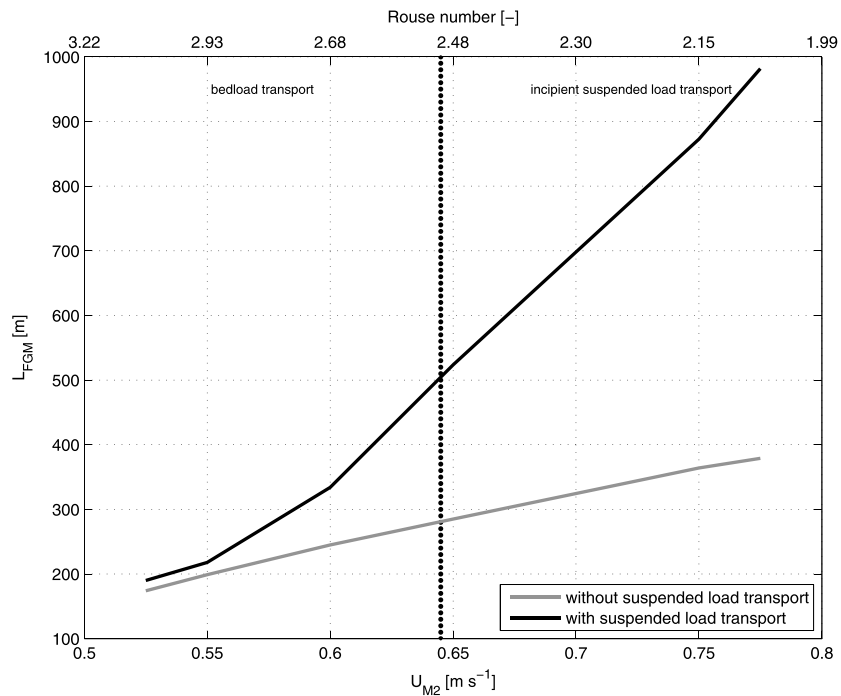
Figure 10. Fastest-growing model (L_{FGM}) for a variation in flow velocity amplitude U_{M2} (m s^{-1}) and hence Rouse number P [−] for a grain size $d = 0.3$ mm and a mean water depth $H_0 = 25$ m. Distinction is made between model simulations without suspended load transport (gray line) and with suspended load transport (black line). The dotted black line separates the bed load transport regime and the incipient suspended load transport regime.

6. Conclusions

Analysis of field data on sand wave occurrence showed that sand wave fields were only found where bed load transport was the dominant transport mode. At locations where suspended load transport was the dominant transport regime, sand wave fields were absent. The lower limit of sand wave occurrence was found at a Rouse number $P = 1.9$.

Model simulations with the numerical process-based geomorphological model Delft3D showed that the damping effect of suspended load transport was caused by the phase lag between the suspended sediment concentrations and the sand wave, resulting in a tide-averaged divergence of suspended load transport at the sand wave crest and hence sand wave decay. For relatively large grain sizes (the bed load regime) the preferred wavelength of the sand wave increased by including suspended load transport. However, for a relatively small grain size (the suspended load regime), the damping effect of suspended load transport in combination with slope-induced transport dominated over the growth mechanism due to bed load transport leading to a stable flat bed.

Previous model studies in which suspended sediment dynamics were included showed a positive growth rate for long sand waves. Alternatively, model simulations in this paper showed that suspended load transport in combination with an advanced turbulence model suppressed very long sand waves, resulting in a finite range of wavelengths of sand waves that experienced growth. Based on this result, critical conditions for sand wave occurrence were found in the model by varying the flow velocity amplitude and grain size independently. The simulations showed that sand waves were only formed for Rouse numbers $P > 2.0$, a value which was comparable to the field observations.

References

Apotsos, A., G. Gelfenbaum, and B. Jaffe (2011), Process based modeling of tsunami inundation and sediment transport, *J. Geophys. Res., 116*, F01006, doi:10.1029/2010JF001797.

Besio, G., P. Blondeaux, and G. Vittori (2006), On the formation of sand waves and sand banks, *J. Fluid Mech., 557*, 1–27, doi:10.1017/S0022112006009256.

Besio, G., P. Blondeaux, M. Brocchini, S. J. M. H. Hulscher, D. Idier, M. A. F. Knaapen, A. A. Németh, P. C. Roos, and G. Vittori (2008), The morphodynamics of tidal sand waves: A model overview, *Coastal Eng.*, 55, 657–670, doi:10.1016/j.coastaleng.2007.11.004.

Best, J. (2005), The fluid dynamics of river dunes: A review and some future research directions, *J. Geophys. Res.*, 110, F04S01, doi:10.1029/2004JF000218.

Blondeaux, P., and G. Vittori (2005a), Flow and sediment transport induced by tide propagation: 1. The flat bottom case, *J. Geophys. Res.*, 110, C07020, doi:10.1029/2004JC002532.

Blondeaux, P., and G. Vittori (2005b), Flow and sediment transport induced by tide propagation: 2. The wavy bottom case, *J. Geophys. Res.*, 110, C08003, doi:10.1029/2004JC002545.

Borsje, B. W., M. B. De Vries, T. J. Bouma, G. Besio, S. J. M. H. Hulscher, and P. M. J. Herman (2009a), Modelling bio-geomorphological influences for offshore sand waves, *Cont. Shelf Res.*, 29, 1289–1301, doi:10.1016/j.csr.2009.02.008.

Borsje, B. W., S. J. M. H. Hulscher, P. M. J. Herman, and M. B. De Vries (2009b), On the parameterization of biological influences on offshore sand wave dynamics, *Ocean Dyn.*, 59, 659–670, doi:10.1007/s10236-009-0199-0.

Borsje, B. W., P. C. Roos, W. M. Kranenburg, and S. J. M. H. Hulscher (2013), Modelling sand wave formation in a numerical shallow water model: The role of turbulence formulation, *Cont. Shelf Res.*, 60, 17–27, doi:10.1016/j.csr.2013.04.023.

Buijsman, M. C., and H. Ridderinkhof (2008), Long-term evolution of sandwaves in the Marsdiep inlet. I: High-resolution observations, *Cont. Shelf Res.*, 28, 1190–1201, doi:10.1016/j.csr.2007.10.011.

Burchard, H., et al. (2008), Observational and numerical modeling methods for quantifying coastal ocean turbulence and mixing, *Prog. Oceanogr.*, 76, 399–442, doi:10.1016/j.pocean.2007.09.005.

Chen, H. Y., and C. F. Nordin (1976), Temperature effects in the transition from dunes to plane bed, M.R.D. Sediment Series, no. 14, US Army Engrs. District, Missouri River Div.

Cherlet, J., G. Besio, P. Blondeaux, V. van Lancker, E. Verfaillie, and G. Vittori (2007), Modeling sand wave characteristics on the Belgian Continental Shelf and in the Calais-Dover Strait, *J. Geophys. Res.*, 112, C06002, doi:10.1029/2007JC004089.

Colombini, M. (2004), Revisiting the linear theory of sand wave formation, *J. Fluid Mech.*, 502, 1–16, doi:10.1017/S0022112003007201.

Deltares (2014), User manual Delft3D FLOW, Deltares (www.deltares.nl), Delft, The Netherlands.

Engelund, F., and J. Fredsøe (1982), Sediment ripples and dunes, *Annu. Rev. Fluid Mech.*, 14, 13–37.

Ernstsen, V. B., R. Noormets, C. Winter, D. Hebbeln, A. Bartholoma, B. W. Flemming, and J. Bartholdy (2005), Development of subaqueous barchanoid-shaped dunes due to lateral grain size variability in a tidal inlet channel of the Danish Wadden Sea, *J. Geophys. Res.*, 110, F04S08, doi:10.1029/2004JF000180.

Fredsøe, J., and R. Deigaard (1992), Mechanics of coastal sediment transport, World Scientific.

Hulscher, S. J. M. H. (1996), Tidal-induced large-scale regular bed form patterns in a three-dimensional shallow water model, *J. Geophys. Res.*, 101, 727–744.

Hulscher, S. J. M. H., and C. M. Dohmen-Janssen (2005), Introduction to special section on marine sand wave and river dune dynamics, *J. Geophys. Res.*, 110, F04S01, doi:10.1029/2005JF000404.

Hulscher, S. J. M. H., and G. M. Van den Brink (2001), Comparison between predicted and observed sand waves and sand banks in the North Sea, *J. Geophys. Res.*, 106(C5), 9327–9338.

Huntley, D. A., J. M. Huthnance, M. B. Collins, C. L. Liu, R. J. Nicholls, R.J. and C. Hewitson (1993), Hydrodynamics and sediment dynamics of North Sea sand waves and sand banks, *Philos. Trans. R. Soc. London, Ser. A*, 343, 461–474.

Komarova, N. L., and S. J. M. H. Hulscher (2000), Linear instability mechanisms for sand wave formation, *J. Fluid Mech.*, 413, 219–246.

Kostaschuk, R. A. (2000), A field study of turbulence and sediment dynamics over subaqueous dunes with flow separation, *Sedimentology*, 47, 519–531.

Kostaschuk, R. A., and P. V. Villard (1996), Flow and sediment transport over large subaqueous dunes: Fraser River, Canada, *Sedimentology*, 43, 849–863.

Lesser, G. R., J. A. Roelvink, J. A. T. M. van Kester, and G. S. Stelling (2004), Development and validation of a three-dimensional morphological model, *Coastal Eng.*, 51, 883–915, doi:10.1016/j.coastaleng.2004.07.014.

McCave, I. N. (1971), Sand waves in the North Sea off the coast of Holland, *Mar. Geol.*, 10, 199–225.

Németh, A. A., S. J. M. H. Hulscher, and H. J. De Vriend (2003), Offshore sand wave dynamics, engineering problems and future solutions, *Am. Gas J.*, 230, 67–69.

Németh, A. A., S. J. M. H. Hulscher, and R. M. J. Van Damme (2007), Modelling offshore sand wave evolution, *Cont. Shelf Res.*, 27, 713–728, doi:10.1016/j.csr.2006.11.010.

Rodi, W. (1984), *Turbulence Models and Their Application in Hydrodynamics: A State of the Art Review*, Univ. of Karlsruhe, Karlsruhe, Germany.

Rubin, D. M., and D. S. McCulloch (1980), Single and superimposed bedforms: A synthesis of San Francisco Bay and flume observations, *Sediment. Geol.*, 26, 207–231.

Sekine, M., and G. Parker (1992), Bed-load transport on transverse slope, *J. Hydraul. Eng.*, 118, 513–535.

Sterlini, F. M., S. J. M. H. Hulscher, and D. M. Hanes (2009), Simulating and understanding sand wave variation: A case study of the Golden Gate sand waves, *J. Geophys. Res.*, 114, F02007, doi:10.1029/2008JF000999.

Terwindt, J. H. J. (1971), Sand waves in the Southern Bight of the North Sea, *Mar. Geol.*, 10, 51–67.

Tobias, C. J. (1989), Morphology of sand waves in relation to current, sediment and wave data along the Eurogeul, North Sea, Report GEOPRO 1989.01, University of Utrecht, The Netherlands.

Van Alphen, J. S. L. J., and M. A. Damoiseaux (1989), A geomorphological map of the Dutch shoreface and adjacent part of the continental shelf, *Geol. Mijnbouw*, 68, 433–444.

Van den Berg, J., F. Sterlini, S. J. M. H. Hulscher, and R. Van Damme (2012), Non-linear process based modelling of offshore sand waves, *Cont. Shelf Res.*, 37, 26–35, doi:10.1016/j.csr.2012.01.012.

Van Oyen, T., and P. Blondeaux (2009), Tidal sand wave formation: Influence of graded suspended sediment transport, *J. Geophys. Res.*, 114, C07004, doi:10.1029/2008JC005136.

Van Rijn, L. C. (1993), *Principles of Sediment Transport in Rivers, Estuaries and Coastal Seas*, Aqua Publications, Amsterdam.

Van Rijn, L. C. (2007), Unified view of sediment transport by currents and waves, Part II: Suspended transport, *J. Hydraul. Eng.*, 133, 668–689, doi:10.1061/(ASCE)0733-9429(2007)133:6(668.

Van Rijn, L. C., D. J. R. Walstra, and M. Van Ormondt (2004), Description of TRANSPOR 2004 (TR2004) and implementation in DELFT3D online, Rep. Z3748, Delft Hydraulics, Delft, The Netherlands.

Van Santen, R. B., H. E. de Swart, and T. A. G. P. van Dijk (2011), Sensitivity of tidal sand wavelength to environmental parameters: A combined data analysis and modeling approach, *Cont. Shelf Res.*, 31, 966–978, doi:10.1016/j.csr.2011.03.003.

Verboom, G. K., and A. Slob (1984), Weakly-reflective boundary conditions for two-dimensional water flow problems, *Adv. Water Res.*, 7, 192–197.